

Laser powder bed fusion of Cu/17-4 PH multi-material system: Microstructural evolution and structure-property relationships

Original

Laser powder bed fusion of Cu/17-4 PH multi-material system: Microstructural evolution and structure-property relationships / Felicioni, S., Crachi, M., Lusicini, D., Sesana, R., Pizzarelli, M., Pavese, M., Bondioli, F.. - In: JOURNAL OF MATERIALS RESEARCH AND TECHNOLOGY. - ISSN 2238-7854. - 43:(2026), pp. 357-372.
[10.1016/j.jmrt.2026.06.063]

Availability:

This version is available at: 11583/3011989 since: 2026-06-12T14:05:55Z

Publisher:

Elsevier

Published

DOI:10.1016/j.jmrt.2026.06.063

Terms of use:

This article is made available under terms and conditions as specified in the corresponding bibliographic description in the repository

Publisher copyright

(Article begins on next page)



Contents lists available at ScienceDirect

Journal of Materials Research and Technology

journal homepage: www.elsevier.com/locate/jmrt

Laser powder bed fusion of Cu/17-4 PH multi-material system: Microstructural evolution and structure-property relationships

Stefano Felicioni^{a,*}, Matteo Crachi^c, Delio Luscinì^c, Raffaella Sesana^c, Marco Pizzarelli^d, Matteo Pavese^{b,a}, Federica Bondioli^{b,a}

^a National Interuniversity Consortium of Materials Science and Technology (INSTM), Via G. Giusti 9, 50121, Firenze, Italy

^b Department of Applied Science and Technology (DISAT), Politecnico di Torino, Corso Duca degli Abruzzi 24, 10129, Torino, Italy

^c Department of Mechanical and Aerospace Engineering (DIMEAS), Politecnico di Torino, Corso Duca degli Abruzzi 24, 10129, Turin, Italy

^d Italian Space Agency (ASI), Via del Politecnico, 00133, Rome, Italy

ARTICLE INFO

Keywords:

Additive manufacturing (AM)
Multi-material additive manufacturing (MMAM)
Metal matrix composite (MMC)
Laser powder bed fusion (LPBF)

ABSTRACT

The integration of copper alloys with high-strength steels through laser powder bed fusion (LPBF) offers a promising pathway toward multifunctional components combining superior thermal conductivity and mechanical performance. However, conventional bimetallic steel/Cu architectures fabricated by sequential deposition often suffer from interfacial defects arising from the large mismatch in thermophysical properties and the intrinsic immiscibility of the Cu–Fe system. In this work, a Cu/17-4 PH multi material system was developed via mechanical powder mixing and processed by LPBF to promote a more homogeneous distribution of phases and mitigate sharp compositional gradients at the interface. Exploiting the rapid solidification conditions inherent to LPBF, the study investigates the extent of partial alloying, solute trapping, and microstructural refinement occurring within this pseudo-alloy. A comprehensive microstructural investigation, together with a deep mechanical characterization at the nanoscale, was performed to elucidate phase distribution, interfacial morphology, and diffusion-driven interactions between the Cu-rich matrix and the Fe-rich reinforcing phase. Nanoscale mechanical testing and thermal characterization, including evaluation of the thermal conductivity, were conducted to establish correlations between processing parameters, microstructure, and functional properties. The results demonstrated the potential of the powder mixing approach to engineer novel high thermal conductivity systems offering an improved trade-off between functional and mechanical performance for advanced thermal management and high-temperature applications.

1. Introduction

Within the continuous evolution of aerospace manufacturing, increasing the service life of critical components remains a central objective. Spacecraft typically rely on liquid-propellant rocket engines which, despite their high performance, are inherently limited by a relatively low number of firing cycles. Among the various elements of these complex assemblies, particular emphasis must be placed on the thrust chamber, due to its critical structural and thermal loading conditions. Within this component the propellant mixture ignites and burns, generating high-velocity exhaust gases that create thrust to propel the rocket. The thrust chamber operates under extremely harsh operating conditions, among the most demanding in engineering applications, as it is subjected to pressures easily exceeding 100 bar and temperatures

greater than 3000 K [1].

To withstand these extreme operating environments, modern liquid rocket engines commonly employ double-walled thrust chambers with regenerative cooling [2]. In this configuration (Fig. 1), one of the propellants, typically the fuel, is routed through a large array of narrow cooling passages, often featuring a rectangular shape. Traditionally, these channels are machined along the profile of a comparatively thick chamber wall, forming an inner liner that separates the circulating coolant from the high-temperature combustion gases, as well as radial ribs that divide adjacent channels. An external jacket is then attached to the ribs using joining techniques such as brazing or electroforming. It is important to note that the materials used for the inner liner and the outer jacket are usually not the same [2].

For this reason, design strategies that integrate multiple metals

* Corresponding author.

E-mail address: stefano.felicioni@polito.it (S. Felicioni).

<https://doi.org/10.1016/j.jmrt.2026.06.063>

Received 7 May 2026; Received in revised form 5 June 2026; Accepted 6 June 2026

Available online 10 June 2026

2238-7854/© 2026 Published by Elsevier B.V. This is an open access article under the CC BY-NC-ND license (<http://creativecommons.org/licenses/by-nc-nd/4.0/>).

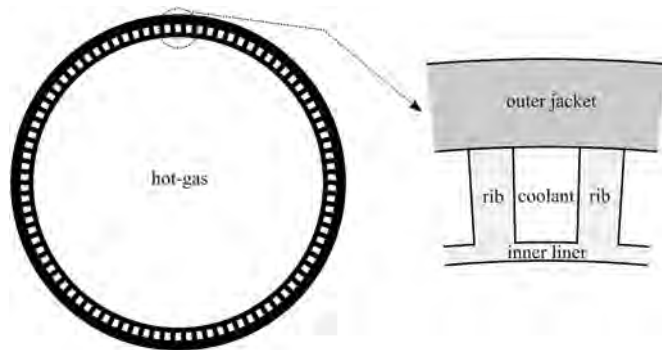


Fig. 1. Schematic cross-sectional view of a regeneratively cooled double-walled thrust chamber [1].

within a single component make it possible to combine properties that would otherwise be physically incompatible. In fact, by selectively placing different materials, components can be engineered to exhibit location-specific characteristics such as enhanced wear resistance, improved corrosion protection, or superior thermal conductivity [3], [4], [5], [6], [7]. As early as the 1970s, NASA implemented multi-metal concepts in the Main Combustion Chamber of the RS-25 engine (formerly known as Space Shuttle Main Engine), where a copper-alloy liner featuring conformal cooling passages was paired with a nickel outer shell, resulting in a highly integrated composite structure, where the copper based material effectively limits the temperature of the wall exposed to the hot gases, enhancing heat transfer away from the combustion region [8]. However, producing such hybrid structures using traditional manufacturing methods presents significant technical obstacles and high production costs [9].

In recent years, advanced additive manufacturing (AM) techniques have provided solutions to these limitations. In particular, laser-based powder bed fusion (LPBF) enables the fabrication of complex three-dimensional metallic components composed of multiple materials, with spatially controlled material placement in all three dimensions [10]. Moreover, it is worth noting that efficient multi-material architectures can also be achieved by combining different AM techniques. For instance, in applications such as additively manufactured rocket thrust chambers, LPBF is used for the fabrication of the inner copper alloy components, while directed energy deposition (DED) processes are typically employed for the deposition of outer structural features [11]. LPBF and DED belong to the class of rapid solidification processes, characterized by extremely high cooling rates (on the order of 10^5 – 10^6 K/s for LPBF), which promote non-equilibrium solidification phenomena and enable enhanced solute trapping, metastable phase formation, and localized alloying effects [12]. As a result, designers gain unprecedented flexibility in both material selection and structural configuration.

Within this framework, the past decade has seen the exploration of several multi-metal architectures, with particular emphasis on copper-based systems. NASA, for instance, is currently manufacturing with AM technologies multi-material components that combine CuCrZr or various grades of GRCo alloys with nickel-based superalloys [13], [14].

In parallel, increasing attention over the last five years has been directed toward the integration of copper and its alloys with steels. Among the investigated material pairings, 316L-CuCrZr [15], [16], [17] is the most widely studied, followed by M300-CuCrZr [18], [19] and 316L-CuSn10 [20], [21] systems. Additional, though less extensive, studies have examined combinations such as H13-Cu [22] and M300-Cu [23]. This kind of coupling is of particular interest since the miscibility gap in the solid state existing between Cu and Fe [24] allows to classify the Cu-Fe systems as pseudo alloys [25], where the Fe-rich phase is embedded within a continuous Cu matrix. This microstructural configuration enables the combination of complementary properties, such as the high thermal and electrical conductivity of copper and the

mechanical strength of steel, within a single material system [26], [27], [28].

Most of the studies on these multi material assemblies, are based on the coupling between the two dissimilar materials where a copper alloy part is fabricated on top of a formerly LPBF-produced steel part, then a second steel part was built on top of the copper alloy part to investigate the bimetallic interfacial properties. The bimetallic steel/Cu joint, in general, revealed numerous defects, including cracks due to a significant difference between the thermo-physical properties of the two materials such as coefficient of thermal expansion, melting temperatures, heat capacities, and thermal conductivity [29].

To mitigate these issues, recent studies have investigated the possibility of using additive manufacturing with mixed powder of copper and steels, obtained through mechanical blending or ball milling of elemental powders to obtain a more isotropic distribution of properties [30], [31], [32].

Building on these considerations, the present work explores the development of a Cu/17-4 PH multi-material obtained by additive manufacturing of mechanically mixed powders, evaluating the effects of the rapid solidification characteristic of the LPBF processing on interfacial architecture, solute partitioning and microstructural features. The underlying rationale is to exploit the non-equilibrium solidification conditions to enable complementary precipitation-driven strengthening in both the immiscible phases and to achieve a compatible thermal and microstructural evolution during aging, analogous to the behavior of high-performance Cu-based alloys designed for harsh environments.

Although mechanical performance is often the primary focus for additively manufactured metallic multi-materials, their thermal characteristics are equally critical, particularly in applications involving heat transfer and thermal management systems. A fundamental parameter that characterizes heat conduction in multiphase or heterogeneous materials is the effective thermal conductivity (ETC). This property is strongly influenced by the material's overall composition, the nature and distribution of its constituent phases, and its microstructural features. In multi-material systems, the ETC is governed by several factors, including the intrinsic thermal conductivity of each phase, their spatial arrangement, particle or phase size, and their respective volume fractions [33]. The presence of porosity further reduces thermal performance, as both the amount and morphology of pores adversely impact heat conduction. When heat passes across the interface between different phases, a temperature discontinuity can occur. This phenomenon, known as interfacial thermal resistance, originates from imperfect interfacial contact as well as differences in the thermophysical properties of the adjoining materials, such as coefficients of thermal expansion and bonding characteristics [34]. A specific form of interfacial resistance, termed thermal boundary resistance or Kapitza resistance, arises from mismatches in the vibrational and electronic structures of the two materials. At the interface, heat carriers, whether electrons or phonons, undergo scattering, and their likelihood of transmission depends strongly on the compatibility of energy states across the boundary [35].

For this class of multi-materials, the available literature about the functional properties remains scarce. Moreover, for both base materials considered in the proposed system, the functional properties are strongly affected by the thermal history experienced during processing. For instance, additively manufactured 17-4 PH stainless steel exhibits a different temperature dependence of thermal conductivity compared with its wrought counterpart, as a result of the AM process-induced microstructure [36], [37]. A comparable trend is observed in pure copper, where deviations from conventionally produced material are primarily associated with the characteristic microstructural refinement induced by the LPBF process [38].

On these bases, unlike most previous studies on steel/Cu multi-materials, which have mainly focused on sequentially deposited bimetallic joints or on mechanically mixed Cu-Fe systems primarily assessed in terms of processability and bulk response, the present study investigates the material implications associated with the development of

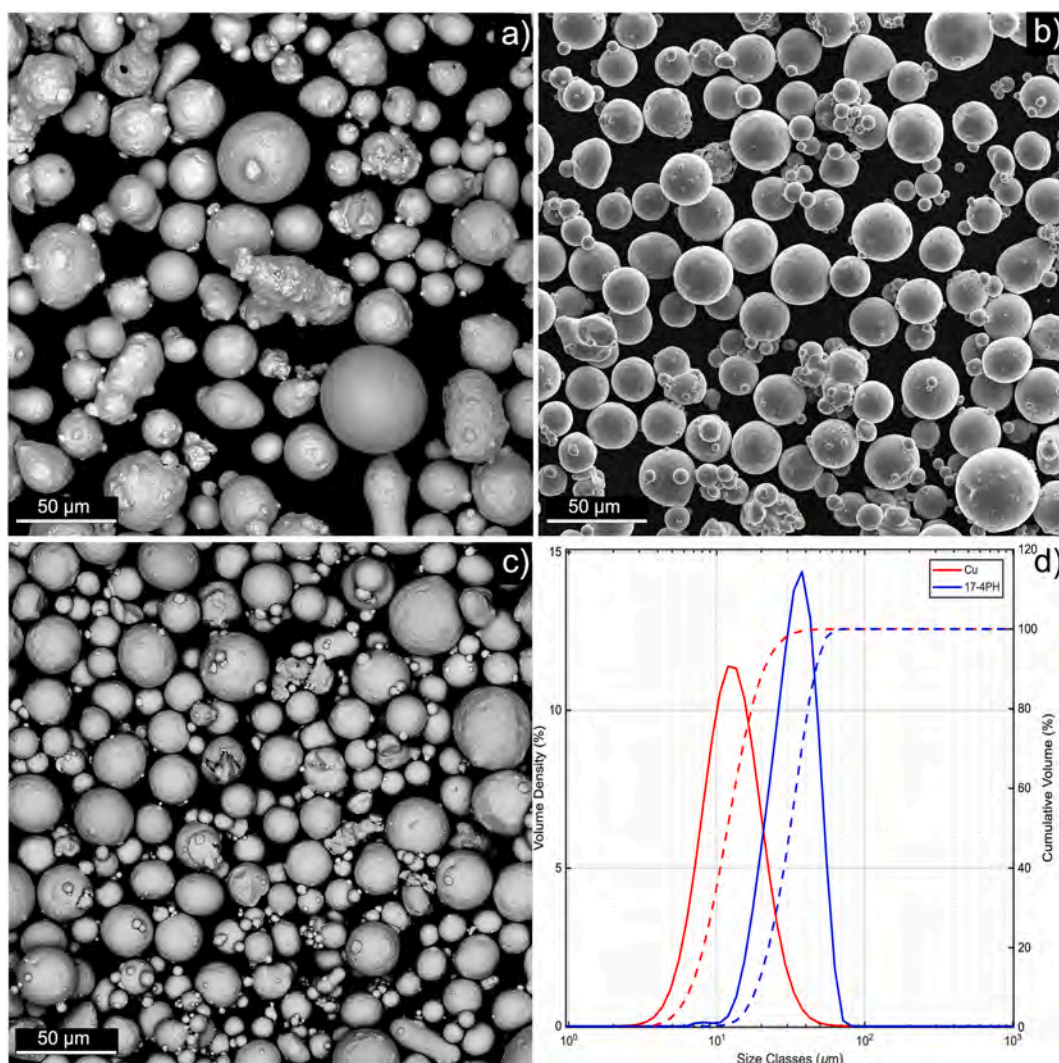


Fig. 2. Morphological SEM observation of a) 17-4 PH steel; b) Cu powder; c) blended composition 80 wt% Cu- 20 wt% 17-4 PH; d) particle size distribution comparison of the constituent powders and the resultant mixture prior to the LPBF process.

high thermal conductivity multi-material systems produced through the powder mixing approach and fabricated through LPBF.

Specifically, it provides a systematic analysis of the resulting interfacial microstructure and mechanical behavior, with particular emphasis on elucidating the metallurgical mechanisms governing diffusion bonding and the interactions between the constituent phases.

To this end, detailed microstructural characterization was carried out to correlate interfacial morphology and phase evolution with the resulting mechanical and functional properties, thereby establishing robust process microstructure and property relationships.

The novelty of the study lies in correlating LPBF induced rapid solidification and thermally activated microstructural evolution with the ETC and mechanical response of the material. This approach enables the thermal behavior to be directly linked to the evolution of the Cu/steel interfacial architecture, providing new insight into the design of Cu/precipitation-hardening stainless steels multi materials for thermal management and high temperature applications.

2. Materials and methods

2.1. Materials

The investigated material is a multi-material, obtained from a powder blend composed of 80 wt% copper and 20 wt% 17-4 PH stainless steel.

The copper powder (reported purity: 99.95%) was supplied by Legor Powmet (LEGOR GROUP s.p.a., Bressanvido, VI, Italy), while the 17-4 PH stainless steel powder was provided by Carpenter Additive (Carpenter Technology Corporation, Philadelphia, PA, USA).

The initial powders were blended using a POWMIX mixer from Sòphia High Tech (SÒPHIA HIGH TECH s.r.l., Somma Vesuviana, NA, Italy) using a process that combines pressurized gas flow with an acoustic pressure field, enabling the preservation of uniform density throughout the mixing stage. Prior to the LPBF process, both the individual powders and the resultant mixture were characterized to define particle size distribution (PSD) and morphology (Fig. 2). For this purpose, a Mastersizer 3000 particle size analyzer (Malvern Panalytical Ltd., Malvern, UK) was used for the PSD, while morphology was assessed by scanning electron microscopy (SEM) observations performed using a Phenom XL benchtop SEM (Thermo Fisher Scientific Inc., Waltham, MA, USA).

As evidenced in Fig. 2d, the starting powders exhibited a consistent difference in PSD. Copper showed $D_{10,3} = 5.9 \mu\text{m}$, $D_{50,3} = 12.6 \mu\text{m}$, and $D_{90,3} = 18.4 \mu\text{m}$, whereas the steel powder presented $D_{10,3} = 19.9 \mu\text{m}$, $D_{50,3} = 33.4 \mu\text{m}$, and $D_{90,3} = 49.7 \mu\text{m}$. This difference was intentionally selected to compensate for the density mismatch between the two materials, thereby improving mixing homogeneity. From a morphological perspective, both powders exhibited a high degree of sphericity (Fig. 2a-b). However, the steel powder showed a greater presence of satellites

Table 1

Constituent powders pycnometer density.

	True Density [g/cm ³]	Std. Dev.
Cu	8,96	0,0367
17-4 PH	7,78	0,0196

Table 2

LPBF process parameters utilized in this work.

P [W]	ss [mm/s]	Hd [mm]	t [mm]	VED [J/mm ³]
250	900	0.105	0.03	88.18

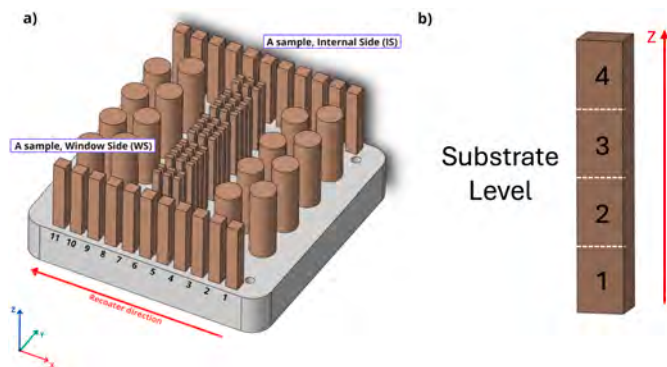


Fig. 3. (a) CAD representation of the building platform showing the arrangement of the samples and the recoater movement direction. Samples are labeled according to the X, Y, and Z reference axes. (b) Schematic representation of the sampling levels along the build direction (Z).

and elongated particles. Despite these morphological differences, no significant effect on flowability was observed, as assessed using the Carr method [39]. Indeed, both powders were classified as exhibiting excellent flowability, with Carr Index (CI) values of 8.79% for the steel powder and 10.78% for the copper powder. Moreover, the morphology of the mixed powder (Fig. 2c) indicates that the mixing procedure did not alter the particle shape or induce noticeable morphological changes.

Finally, the true density of each constituent powder was calculated by means of pycnometry using an AntonPaar Ultracyc 5000 (Table 1), and the optical behavior of the resultant mixture was evaluated by means of a Shimadzu UV-2600 UV-VIS spectrophotometer (Shimadzu Corporation, Kyoto, Japan) fitted with the ISR2600Plus integration sphere which measured an average optical absorption of 40.03% at 1070 nm confirming the processability with infrared (IR) AM setups.

2.2. Experimental

All the specimens were fabricated using a Concept Laser M2 powder bed fusion system, featuring a standard IR laser source and a cubic build envelope of 250 mm in each spatial direction. The machine operates under a controlled nitrogen atmosphere with a filtered gas recirculation system and employs a silicon blade recoating mechanism for powder deposition. The processing parameters adopted in this study, selected on the basis of prior investigations [40], are summarized in Table 2, together with the volumetric energy density (VED), calculated as:

$$VED = \frac{P}{ss \cdot Hd \cdot t} \quad \text{Eq. (1)}$$

where P , ss , Hd , and t represent the laser power, scanning speed, hatching distance, and layer thickness, respectively.

A segmented “island” scanning approach, proprietary to Concept Laser systems, was implemented during fabrication. This strategy divides each layer into smaller sections that are selectively melted in a

non-sequential pattern, promoting a more uniform thermal distribution thanks to the stochastic exposure of these islands.

To evaluate the stability of the composition along the three spatial directions (with Z corresponding to the building direction) while maintaining constant processing parameters, two potential effects were considered: powder sedimentation within the hopper during processing and possible compositional variations induced by the recoater movement along the X direction.

For this purpose, twenty-two identical A-type samples were produced. As illustrated in Fig. 3a, each sample was extracted from a parallelepiped-shaped deposition with a square base of $15 \times 15 \text{ mm}^2$ and a height of 70 mm. The samples were positioned in two rows along the X direction at the peripheral regions of the building platform, following the recoater movement. Each row contained eleven samples and, to distinguish between the two rows, the samples were labeled as Internal Side (IS) and Window Side (WS), as indicated in Fig. 3a.

To further investigate possible compositional variations along the build direction (Z), each parallelepiped sample was sectioned into four distinct levels along its height, as schematically shown in Fig. 3b. These levels allowed the evaluation of potential compositional discretization occurring during the layer-by-layer deposition process.

As a first step in the verification of compositional stability, the densification of the samples was evaluated following ASTM B311-22 [22], applying the Archimedes method. Mass determinations were carried out using a KERN ABS 80-4 N (KERN & SOHN GmbH, Germany) having a resolution of 0.10 mg, equipped with the density measurement setup KERN YDB-03. To ensure the reliability of the density results, and distinguish variations imputable to inherent porosity, a complementary statistical assessment was conducted through quantitative image analysis of selected cross-sections. Specimens were cut along orientations both transverse and longitudinal to the build direction and prepared using conventional metallographic techniques. For each condition, thirty micrographs were acquired at $50\times$ magnification with a Leica DMI 5000 M optical microscope (Leica Microsystems GmbH, Germany). The collected images were subsequently processed and evaluated using ImageJ software.

The phase identification was further validated by means of X-ray diffraction (XRD) measurements on sections perpendicular to the build direction using an Empyrean diffractometer (Malvern Panalytical Ltd., UK) equipped with $\text{Cu K}\alpha$ radiation. The instrument was operated at an accelerating voltage of 40 kV and a current of 40 mA. Diffraction patterns were collected over a 2θ range of $30\text{--}140^\circ$ using a step size of 0.013° . The obtained diffractograms were subsequently processed for phase identification using X'Pert High Score.

To investigate precipitation phenomena and microstructural evolution, the specimens were subjected to direct aging heat treatments (DAHT) at temperatures of 600, 650 and 700°C for durations of 1, and 5 h.

The selection of the appropriate thermal cycle for post-processing was supported by Differential Scanning Calorimetry (DSC) analysis performed using a Mettler Toledo STARE System 3⁺ TGA/DSC instrument (Mettler-Toledo International Inc., Greifensee, Switzerland). Measurements were conducted from ambient temperature up to 1200°C at a heating rate of 10 K min^{-1} under an argon atmosphere. In addition, the specific heat capacity (C_p) was determined by Sinusoidal Modulated Temperature Differential Scanning Calorimetry (SMT-DSC) using a Hitachi Nexta DSC 600 instrument (Hitachi Ltd., Tokyo, Japan), with the same heating rate up to 700°C following the ASTM E2716 standard [41].

The thermal conductivity of the as-built samples (λ) was determined by means of the Laser Flash Method using a Micro Flash 457 apparatus (NETZSCH Group AG, Germany) on samples with dimensions of $10.0 \times 10.0 \times 2.0 \text{ mm}^3$. This technique provides the thermal diffusivity (α) of the material. The ETC was subsequently calculated according to the relation derived from Fourier's law :

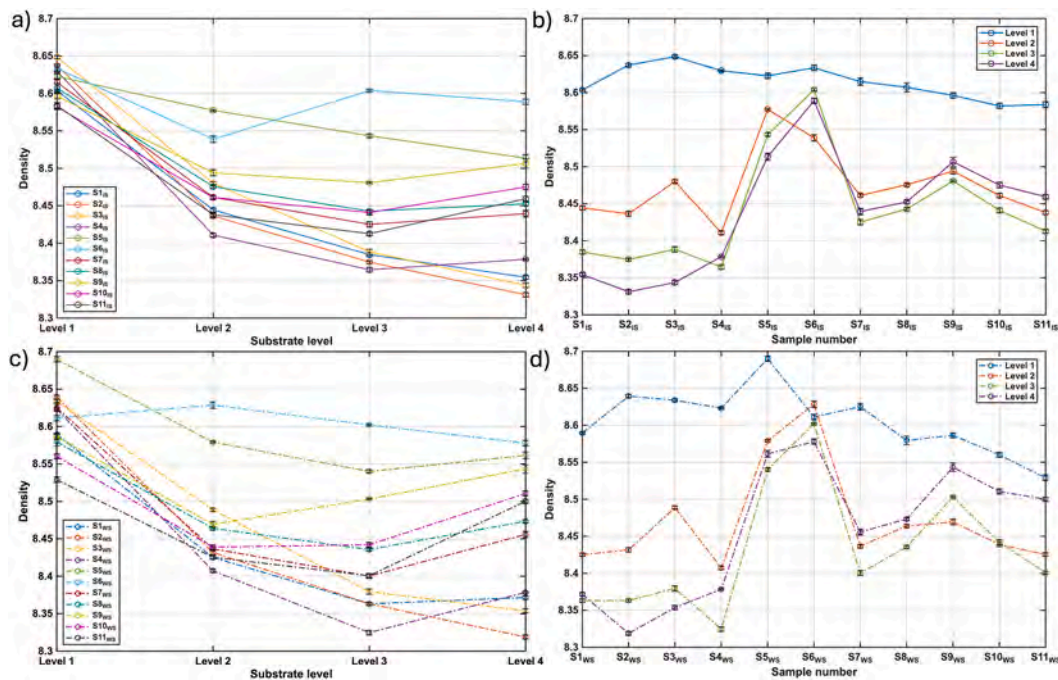


Fig. 4. Archimede's density distribution of IS and WS samples as a function of build height (Z) and position along the recoater direction (X): a), c) Variation along the build direction; b), d) Spatial distribution along the recoater direction at each level.

$$\lambda = \alpha \cdot \rho \cdot C_p \quad \text{Eq. (2)}$$

where ρ is the bulk density and C_p is the specific heat capacity.

For microstructural characterization, both as-built (AB) and heat-treated specimens required chemical etching to clearly reveal structural features. Grain morphology was exposed using an aqueous solution composed of 1.5 g FeCl_3 , 10 ml HCl , and 30 ml ethanol, for time between 2 and 5 s.

Further investigation of precipitate morphology and overall microstructural features was carried out using scanning electron microscopy (SEM). Analyses were performed with a TESCAN S9000G system (Tescan Group a.s., Czech Republic) fitted with electron backscatter diffraction (EBSD) capabilities. EBSD measurements enabled the determination of mean grain size and median misorientation angle. The acquired datasets were processed using Aztec Crystal software (Oxford Instruments plc., UK). Grain boundaries were identified as interfaces exhibiting misorientation angles exceeding 15° , whereas boundaries with lower angular deviation were classified as sub-grain boundaries.

Finally, on the same samples, the overall mechanical response of the material was investigated at multiple length scales in order to evaluate the influence of diffusion phenomena on the mechanical stability of the MMC. Vickers hardness measurements were first performed using an INNOVATEST NEMESIS 9000 hardness tester (INNOVATEST Europe BV, Maastricht, The Netherlands) equipped with the Impressions XTTM control system. The tests were conducted on the same specimens prepared for microstructural observations with a load of 1 kg within a dwell time of 15 s. Hardness measurements were carried out on both planes parallel and perpendicular to the building direction of each sample, with ten independent indentations performed on each surface. To avoid interactions between adjacent plastic deformation fields, the spacing between indentations was maintained at a minimum of three times the diagonal length of the imprint.

Then, nanoindentation tests were conducted to probe the local mechanical properties of the interfacial regions where liquid-phase reactions occurred. These measurements were performed in accordance with ISO 14557 [42] using a Bruker TI 950 nano indenter (Bruker Nano Surfaces, Minneapolis, MN, USA) equipped with a Berkovich diamond tip and operated in load-control mode at room temperature. For

hardness and modulus determination, the indenter was loaded up to a maximum load of 3 mN with loading and unloading rates of $300 \mu\text{N/s}$, followed by a holding time of 5 s at peak load. A total of 256 indentations were performed following a 16×16 grid arrangement with a spacing of $5 \mu\text{m}$ to prevent overlap of the plastically deformed regions. The resulting load displacement curves were analyzed using a dedicated software.

3. Results and discussion

3.1. Compositional stability and densification behavior

Despite the challenges associated with the processing of Cu with IR laser sources the samples exhibited a remarkable densification degree as confirmed by the densification calculation both via buoyancy methods and imaging. Fig. 4 reports the density calculated in the three directions extracted using Archimede's method.

Taking as a reference the theoretical density of 8.77 g/cm^3 , calculated from the rule of mixtures using pycnometer-measured powder densities (Table 1), all the samples exhibit a slight lower measured density, indicating the presence of residual porosity typical of LPBF-processed materials.

From Fig. 4a-c, a general decreasing trend in density along the build direction (Z) can be observed for most samples. The density drops from Level 1 ($\approx 8.60 - 8.65 \text{ g/cm}^3$) to Level 3 ($\approx 8.37 - 8.40 \text{ g/cm}^3$), followed by a slight stabilization at Level 4.

Considering that 17-4 PH steel has a lower density than copper, this trend reflects a progressive enrichment in steel content with increasing build height. A behavior that is consistent with the powder segregation within the hopper, where the denser Cu particles tend to sediment toward the bottom, while the relatively lighter steel particles become enriched in the upper regions of the powder bed over time. As the build progresses layer by layer, this leads to a time-dependent compositional drift, with later deposited layers containing a higher fraction of steel and thus exhibiting lower density. This effect is most pronounced between Level 1 and Level 3, where the maximum compositional deviation, corresponds to a density difference of approximately 0.30 g/cm^3 ($\approx 3.6\%$ relative to the theoretical value).

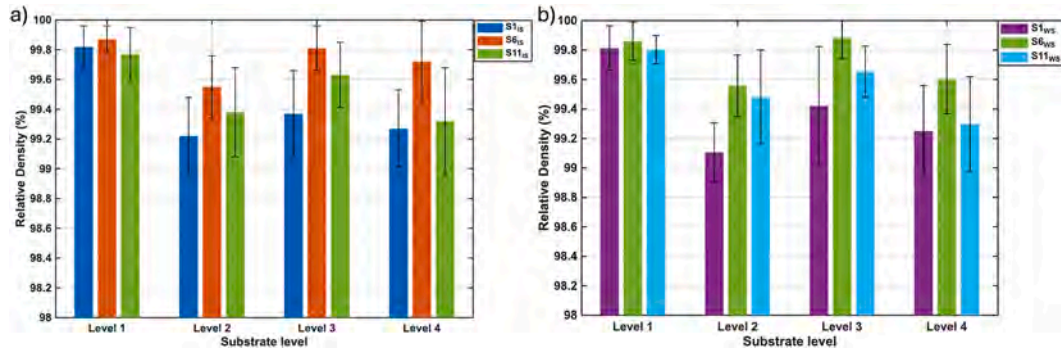


Fig. 5. Imaging defectiveness evolution along the build direction (Z) for IS (a) and WS(b) batches, evaluated on representative samples (S1, S6, S11) supporting the compositional origin of the observed density variations.

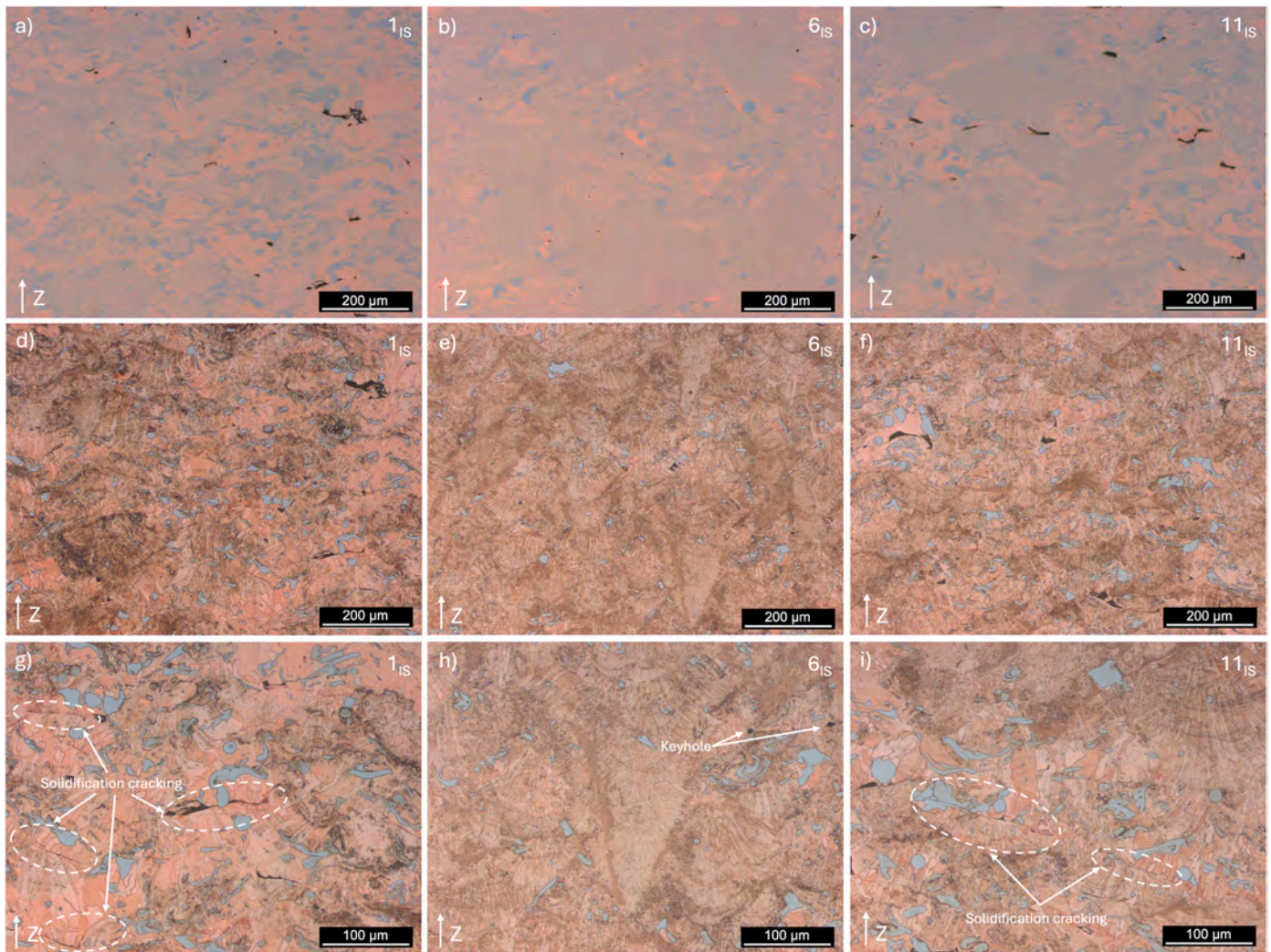


Fig. 6. Optical micrographs of samples 1IS, 6IS, and 11IS, selected as representative locations along the recoater direction, acquired at different magnifications before etching (a–c) and after etching, illustrating the phase distribution and defect morphology.

Focusing instead on Fig. 4b and d, which describe the spatial variation along the recoater direction (X), at each level, density values are not completely uniform, with slightly higher densities observed in central samples (e.g. S5_{IS} and S6_{IS}), and lower values toward the edges. This suggests that the recoater movement may induce a minor lateral redistribution of the powder blend, possibly due to differences in spreading dynamics or particle mobility.

In contrast, no significant compositional variation is observed along the transverse (Y) direction. The samples produced under both IS (Fig. 4aandb) and WS conditions (Fig. 4candd) display very similar density trends, indicating that any potential compositional gradient along Y is negligible compared to the variations observed in the other directions.

To support the interpretation of density variations as primarily

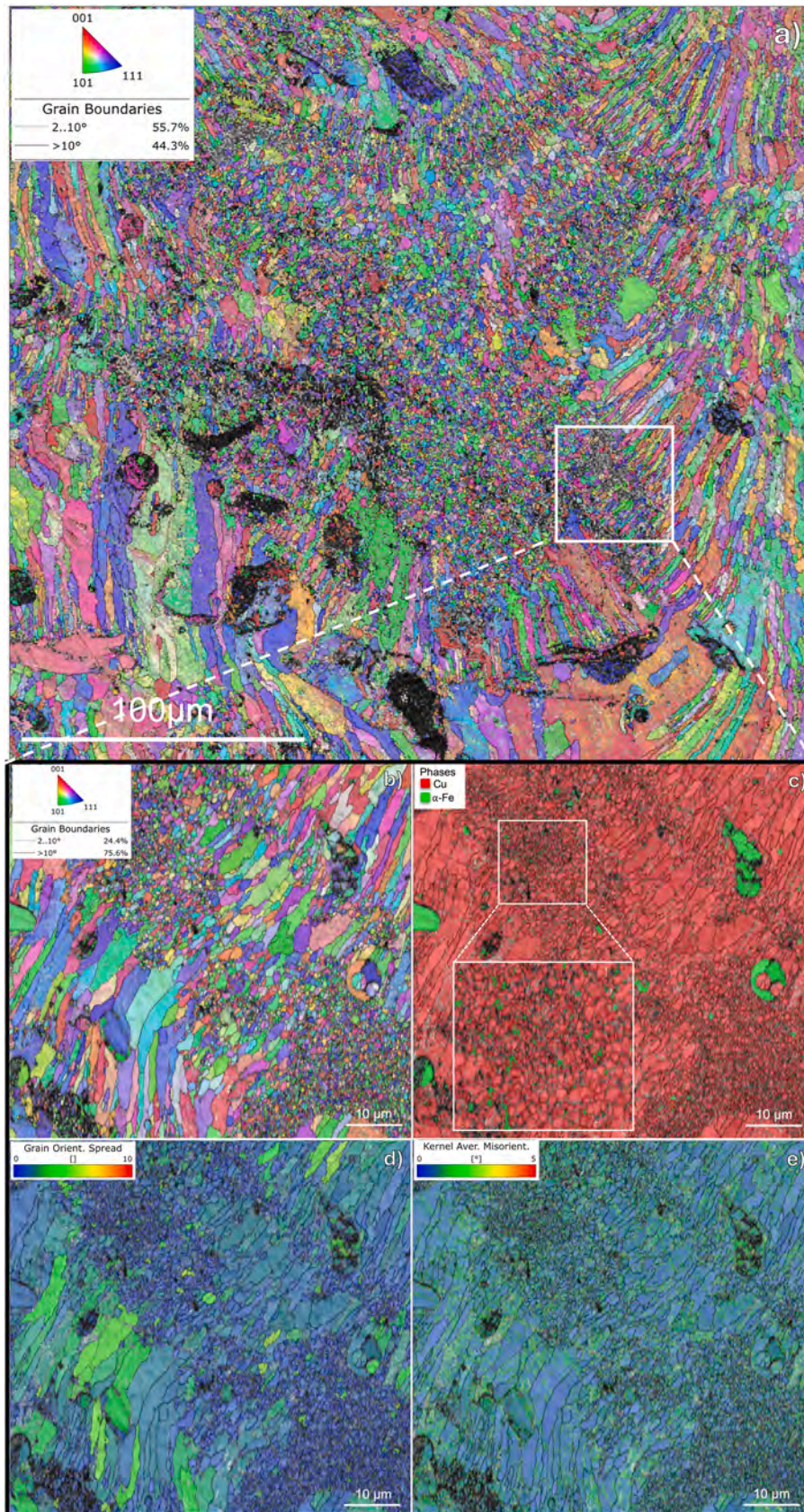


Fig. 7. EBSD mapping of the 615 sample showing microstructural morphology at different magnifications: (a) inverse pole figure (IPF) map of a keyhole melt pool; (b) higher-magnification IPF map along the melt pool boundary, highlighting the columnar-to-equiaxed transition (CET); (c) phase distribution corresponding to the area shown in (b); (d) grain orientation spread (GOS) map of the same region; and (e) kernel average misorientation (KAM) map of the same region.

compositional rather than defect-related, the defectiveness level was quantitatively evaluated via image analysis for both sample batches (IS and WS). Since the recoater motion was found to have a limited influence on density variation, three representative samples along the X direction (S1, S6, and S11) were selected for each batch and analyzed across all build levels.

The results, reported in Fig. 5, indicate that defectiveness remains essentially constant along the build direction (Z) for all the investigated samples, with only a marginally higher densification degree observed during the initial deposition stages. Furthermore, sample S6 consistently exhibited a lower degree of defectiveness than S1 and S11 in both batches, which helps explain the comparatively higher density values registered in the central samples of Fig. 4b–d. Therefore, while recoater-induced effects appear to have a limited impact on composition, they may still contribute to localized variations in defect formation, with central regions benefiting from more stable powder spreading conditions.

To better understand the nature of the defectiveness and enable a direct assessment of the spatial distribution of the Cu-steel phases, Fig. 6 presents representative cross-sectional micrographs of samples S1_{IS}, S6_{IS}, and S11_{IS}, taken as characteristic positions along the recoater direction, both before (Fig. 6a–c) and after etching (Fig. 6d–i). The etching clearly revealed both the grain morphology of the Cu matrix and the melt pool geometry.

At the macroscopic scale, all samples exhibit a continuous Cu-rich matrix embedding large steel-rich islands, together with darker regions associated with deeper melt pools, or frequently located at the intersections between adjacent scan tracks. The spatial distribution of these features, however, is not uniform across the build platform. In particular, the sample S6_{IS} is characterized by a predominance of the darker morphology systematically showing deeper melt pools reflecting a different melting regime compared to the outer regions.

This spatial heterogeneity can be rationalized by considering the interaction between the laser beam delivery system and absorption behavior of the material. In galvanometer based LPBF systems employing f-theta optics, the laser beam is nominally focused across the entire scan field, however, the angle of incidence varies with position [43]. Near the center of the build platform, the beam is nearly normal to the surface, whereas toward the edges it becomes increasingly inclined. As demonstrated by Fathi-Hafshejani et al. [44], this variation causes a variation in the beam shape which leads to a decrease in the effective power density and coupling efficiency of the laser radiation into the material. Moreover, more recent studies demonstrated also a minor effect of the incidence angle on the absorptivity, that has been observed slightly higher under shallow irradiation conditions [45].

This last effect is expected to be especially pronounced in the present system due to the high reflectivity of copper at IR wavelengths. Accordingly, even small variations in incidence angle or local intensity can lead to significant differences in absorbed energy. The observed transition in melt pool morphology, in fact, is consistent with this interpretation. The predominance of darker regions in the central area suggests the establishment of a keyhole melting regime, characterized by deeper and narrower melt pools (Fig. 6e; Fig. 6h), whereas, the outer regions appear to remain predominantly in a conduction mode regime. The transition between these regimes is highly sensitive to peak power density, and therefore small spatial variations in absorbed energy can result in a marked difference in melt pool behavior [46].

The onset of keyhole conditions in the central region also provides a plausible explanation for the observed microstructural refinement (Fig. 6h). Keyhole melting is usually associated with enhanced recoil pressure and vigorous fluid flow within the molten pool, thereby promoting increased turbulence and strong Marangoni convection, driven by surface-tension gradients along the melt pool surface.

Given the extremely steep thermal gradients typical of LPBF, this mechanism induces strong outward flow from the hot center of the melt pool toward the cooler peripheral regions. In the Cu-steel system under

examination, this effect is further amplified by the significant differences in thermophysical properties between the two constituents. Notably, copper exhibits lower melting temperature, and a surface tension with a strong temperature dependency, that is two third that of the iron-rich phases [47], exacerbating Marangoni stresses and driving marked interfacial flow.

These combined effects promote more efficient mixing between the immiscible Cu and steel phases, resulting in a significantly finer dispersion of steel. Conversely, under conduction mode conditions, at the edges of the build platform, the reduced melt pool depth and weaker convective flow limit the redistribution of the steel phase, leading to the formation of larger, and more distinct steel-rich islands.

Furthermore, the preferential localization of the darker regions at track overlaps can be attributed to local energy accumulation due to remelting. These regions are more likely to exceed the threshold for keyhole formation, particularly in areas where the baseline energy input is already elevated, such as the center of the build platform.

Concerning defect formation, three main types of defects can be identified in the selected micrographs: sporadic lack-of-fusion defects, keyhole-induced porosity, and solidification cracking. Their occurrence, however, is function of the melting regime: the S6 condition, representative of deposition in the central region of the build platform, is mainly characterized by fine spherical porosity, which can be associated with keyhole-related gas entrapment. Conversely, solidification cracking represents the predominant defect in the peripheral builds (S1 and S11), where it is mainly observed in the lower regions of the melt pools, as highlighted in Fig. 6g and i.

This preferential localization can be interpreted considering the previously described phase segregation and thermal conditions. As solidification progresses, the steel phase, characterized by a higher melting temperature, solidifies earlier and acts as a local heat sink for the surrounding liquid copper, leading to the development of steep thermal gradients and localized shrinkage stresses within the remaining liquid, which promote crack initiation and propagation. The size and morphology of the defects are therefore strongly dependent on their nature. The spherical pores observed in S6 are the smallest defects, with an average equivalent circle diameter of $3.2 \pm 1.2 \mu\text{m}$. By contrast, solidification cracks and lack-of-fusion defects, being mainly interfacial defects, feature a size that is closely related to the extent of the segregated domains. In the analyzed micrographs, however, their length generally remains below $100 \mu\text{m}$.

3.2. As built microstructural morphology

The effects of the described solidification dynamics on the microstructural evolution are corroborated by Fig. 7, which presents EBSD mapping acquired at different magnifications of sample S6_{IS}. In this region, the refined distribution of steel phases plays a critical role in governing grain nucleation and growth. In particular, the finely dispersed steel particles can potentially act as preferential heterogeneous nucleation sites for the solidifying Cu matrix. This effect arises from the reduction in the critical nucleation energy barrier at the interface between dissimilar phases, which promotes the formation of new grains during solidification [48].

Previous studies on Fe/Cu, have shown favorable crystallographic and interfacial characteristics at Fe/Cu interfaces. For instance, Wang et al. reported, through density functional theory calculations, that γ -Fe/Cu interfaces can exhibit favorable interfacial stability and adhesion, supporting the potential role of Fe-rich phases as heterogeneous nucleation substrates for Cu [49]. Moreover, experimental studies on Cu–Fe systems have reported coherent or semi-coherent Fe-rich/Cu interfaces, including cube on cube orientation relationships between FCC-Fe particles and the Cu matrix, further suggesting crystallographic compatibility between the two phases [50], [51].

Consequently, regions characterized by a finer dispersion of steel may exhibit a significantly higher nucleation density, leading to a

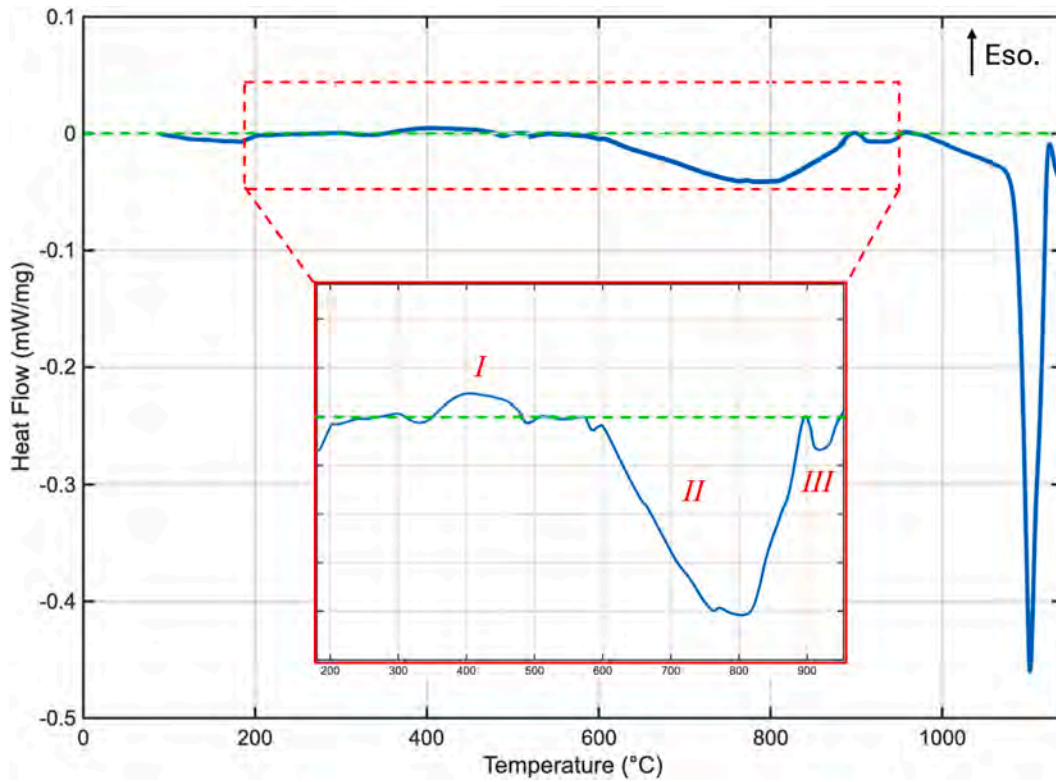


Fig. 8. DSC plot of the as-built samples up to melting.

refined grain structure compared to areas where steel is present as coarse islands. This behavior is particularly evident near the melt pool boundaries, as shown in the phase map of Fig. 7b, where steep thermal gradients and high solidification rates promote this phenomenon. Under these conditions, the combined effect of heterogeneous nucleation and

rapid solidification alters the classical columnar to equiaxed transition (CET) typically observed in LPBF processed materials, which would otherwise favour the formation of columnar grains [52]. The presence of a high density of steel particles, in fact, locally disrupts epitaxial grain growth across melt pool boundaries, inhibiting the competitive growth

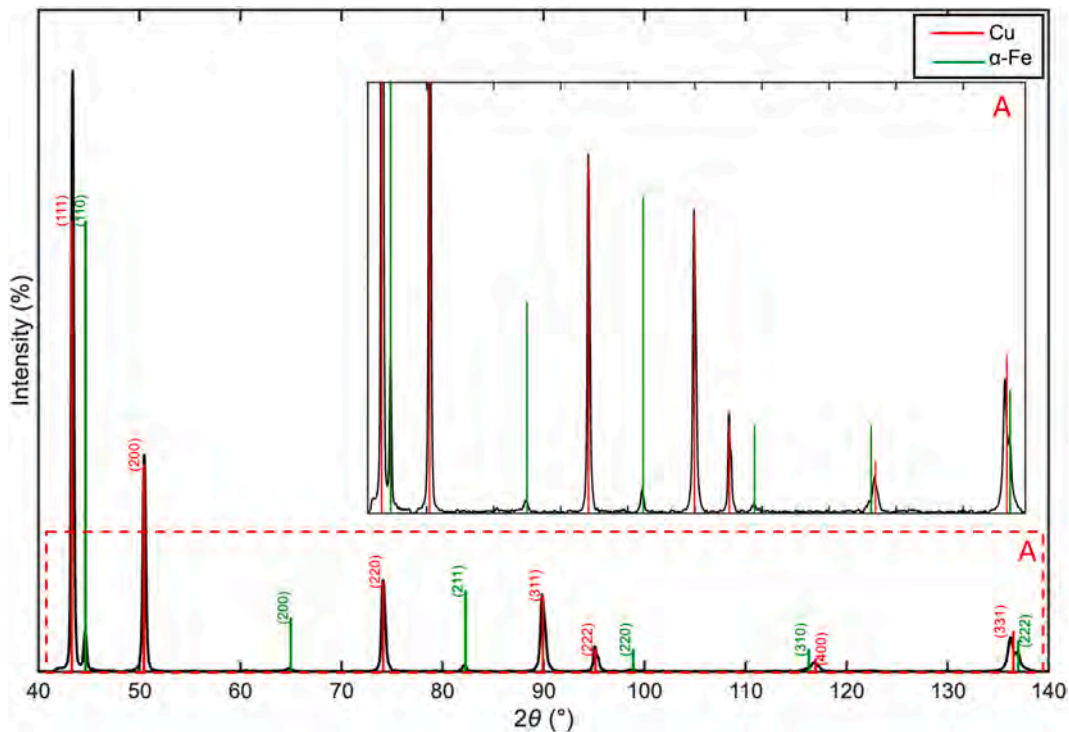


Fig. 9. XRD pattern of sample S6IS in the as-built condition, revealing a fully separated Cu–αFe phase system and the absence of intermetallic compounds, confirming limited mutual solubility and interaction between the two phases.

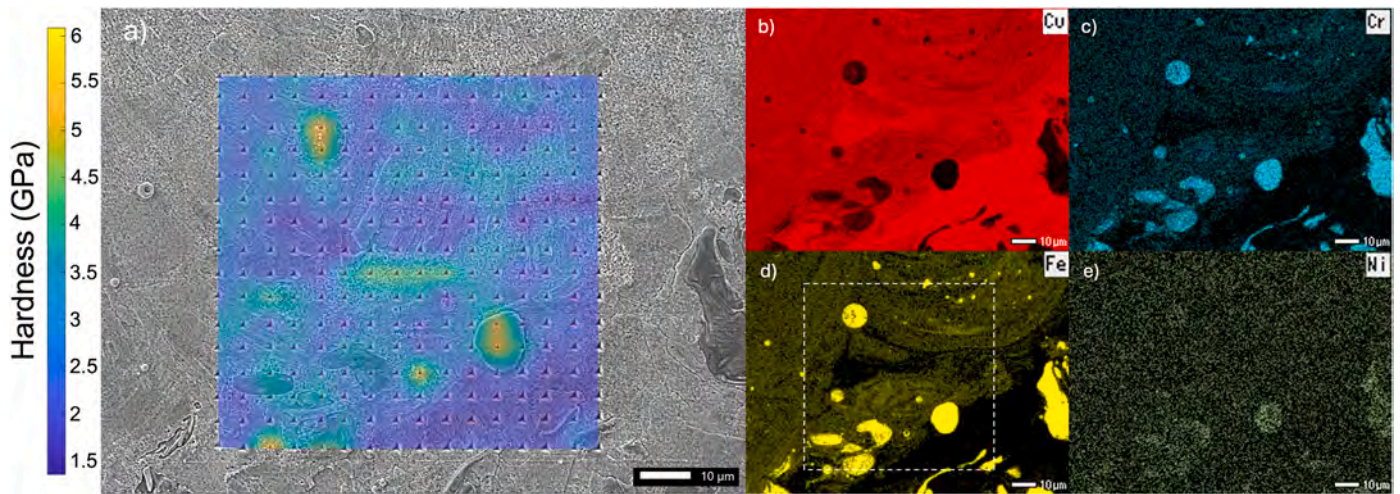


Fig. 10. SEM observation of the nanoindentation mapping across two melt pool interfaces of samples 6_{ws} in as-built condition: a) Indentation shape and hardness response within the different microstructural features; b-e) EDS elemental mapping of the same area.

of favorably oriented grains, promoting instead grain fragmentation and re-nucleation, contributing to the overall grain refinement with an equiaxed morphology tendency.

Additional EBSD-derived parameters such as kernel average misorientation (KAM) and grain orientation spread (GOS), whose maps are reported in Fig. 7d and e, can be considered to enforce the proposed interpretation. While these metrics do not directly relate to the nucleation dynamics, they provide useful information on local lattice distortion and intragranular orientation heterogeneity, respectively.

As visible in Fig. 7d, the finer regions are characterized by lower GOS, indicating reduced intragranular misorientation, a conclusion consistent with a solidification regime dominated by nucleation, where the formation of numerous small grains limits the accumulation of lattice distortion within individual grains. In contrast, coarser regions exhibit higher GOS values, reflecting extended grain growth and increased intragranular strain development. Furthermore, local misorientation (as evidenced by KAM map, Fig. 7e) displayed higher values near the interfaces because of the stronger thermal gradients developed between the two materials, and local constraint effects. This last aspect suggests also the establishment of possible stress induced recrystallization phenomena, definitely contributing to the overall observed microstructural refinement as demonstrated by Xu et al. [53], [54], [55] on Cu–Ni alloys.

3.3. Thermal evolution

To investigate the thermal evolution of the material and evaluate potential precipitation kinetics in the as-built (AB) condition, differential scanning calorimetry (DSC) was carried out to define suitable parameters for post-build heat treatment. The DSC curve (Fig. 8) shows a nearly flat thermal evolution up to approximately 600 °C, with only a weak exothermic phenomenon (peak I) at around 400 °C; above this temperature, however, two more pronounced endothermic events (peaks II–III) can be distinguished.

Due to the attenuated thermal response and the partial overlap between the different contributions, the identification of the thermal events was supported by the analysis of the first derivative of the DSC heat-flow signal. This approach allowed subtle slope variations in the DSC curve to be resolved more clearly and was used to determine the temperature ranges associated with the individual thermal events. Accordingly, the baseline intervals for peak separation were defined by considering the derivative-defined onset and end points of each contribution, enabling a more reliable distinction between the low-temperature exothermic event and the subsequent high-temperature

endothermic phenomena.

The observed thermal evolution agrees well with that reported for additively manufactured 17-4 PH steel and can be interpreted considering the composite nature of the material. Two primary factors govern this behaviour. First, the 17-4 PH phase retains a supersaturated martensitic structure because of the extremely high undercooling degree inherent to the LPBF process. Second, the negligible mutual solubility and limited interdiffusion between Cu and Fe promote pronounced phase separation, such that the Cu-rich matrix and the steel phase evolve largely independently during both solidification and subsequent thermal exposure.

The independent phase evolution is reflected in the fully resolved XRD pattern of Fig. 9 representative of sample S6_{IS} in AB condition. The diffraction data indicate a fully binary phase constitution, consisting exclusively of Cu and α -Fe, with no evidence of intermetallic phase formation, thereby confirming the absence of any chemical interaction between the two constituents.

Going back to the DSC, in the low-temperature range (≈ 400 °C), peak I can be identified and attributed to the precipitation of Cu-rich phases within the supersaturated martensitic regions of the 17-4 PH phase [56], [57]. This process involves the formation of coherent Cu clusters, which progressively evolve into metastable ϵ -Cu precipitates, and constitutes the primary strengthening mechanism of 17-4 PH steel. The pronounced broadening of this peak may also reflect an additional exothermic contribution associated with precipitate growth and coarsening, and the possible formation of Nb-rich secondary phases. However, owing to the relatively low fraction of 17-4 PH in the system and the predominance of the Cu matrix, these transformations appear significantly attenuated in the DSC thermogram.

With respect to the clear endothermic event from 600 to 900 °C (peak II), which may be attributed to the reversion of martensite (α') into austenite (γ) [56], [58], this transformation, typically occurring at lower temperatures in conventional steels [59], appears shifted to higher temperatures due to the local Ni depletion within the steel matrix. Nickel is well known as a strong austenite stabilizer; therefore, its reduced concentration decreases γ -phase stability and consequently raises the temperature required for the $\alpha' \rightarrow \gamma$ transformation. For the considered case, this effect is compounded by the presence of copper. Given the complete mutual solubility between Ni and Cu [60], nickel tends to preferentially partition into Cu-rich regions during solidification and subsequent thermal cycles inherent to the AM process.

This behavior is evidenced by the EDS elemental mapping of Fig. 10, conducted within a representative molten pool, that reports a relatively homogeneous spatial distribution of Ni across the analyzed area.

Table 3

Average microhardness of as-built samples at positions 1, 6, and 11 along the recoater direction (X), averaged over IS and WS batches, highlighting higher hardness at the central position.

	HV1	Std. Dev.
S1	127	12
S6	139	5
S11	125	8

Finally, the last endothermic event can be attributed to the dissolution of the coherent ϵ -Cu precipitation [56], [57] before the melting of the Cu matrix. Under these considerations, the identified thermal evolution suggests that a direct aging heat treatment (DAHT) within the 600–700 °C range can be effectively employed, avoiding the need for a prior solutioning step typically required in conventional processing routes. This approach, that is enabled by the AB microstructural state produced by LPBF, should result in a precipitation-driven strengthening mechanisms of the steel phases crucial in determining the mechanical response.

3.4. Hardness response and aging behavior

Concerning the hardness response, the AB samples exhibit an average microhardness of 130 ± 12 HV, calculated by considering both the IS and WS batches, which were previously demonstrated to be statistically comparable.

Peak hardness values are observed for samples located in the central region of the build platform along the (X) direction. Table 3 reports the average hardness measured at the characteristic positions 1, 6, and 11, showing that the central position (position 6) exhibits not only higher hardness but also a reduced scatter in the measurements. Such trend, can be easily attributed to the combination of the lower defect density and the more homogeneous microstructure evidenced in Figs. 5 and 6.

Focusing on these samples, the nanoindentation mapping in AB condition, offers further insights, revealing a pronounced spatial heterogeneity in hardness, which is consistent with the microstructural variability observed across the melt pools (Fig. 6), particularly in terms of phase distribution and characteristic size.

A representative example is shown in Fig. 10, where hardness mapping is reported for a melt pool boundary region together with the corresponding elemental distribution of the same area (Fig. 10b–e). The

strong spatial correlation between hardness and composition highlights the role of local phase distribution in governing the mechanical response.

This behavior can be rationalized considering both the intrinsic mechanical contrast between the Cu-rich matrix and the steel phase, as well as the strong dependence of hardness on grain size. In similar Cu-steel pseudo alloy systems, it has been shown that the mechanical response is governed by the combined effect of phase fraction and microstructural refinement, with grain size playing a key role through Hall-Petch strengthening [32].

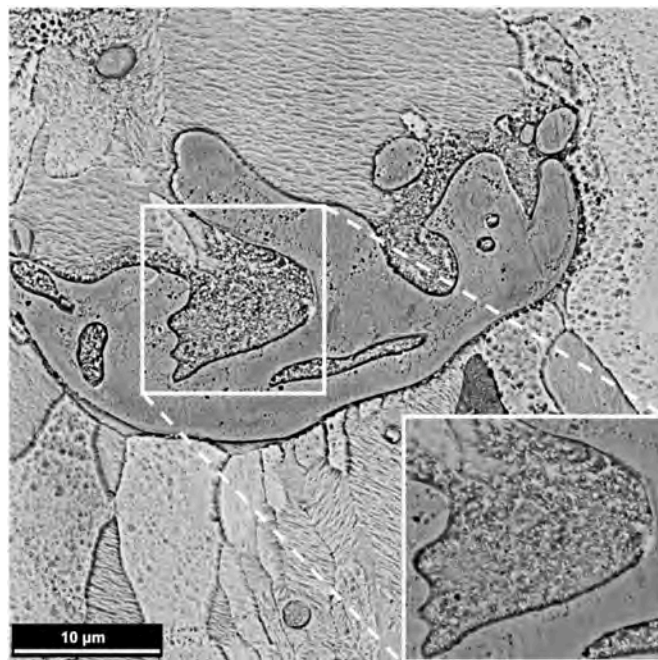


Fig. 12. SEM micrograph of the peak-aged condition of S6_{WS} at 600 °C, showing a steel-rich island surrounded by a dispersion of fine spherical particles. The decoration of the island boundaries highlights diffusion-driven coarsening and solute migration toward larger features, consistent with an Ostwald ripening mechanism.

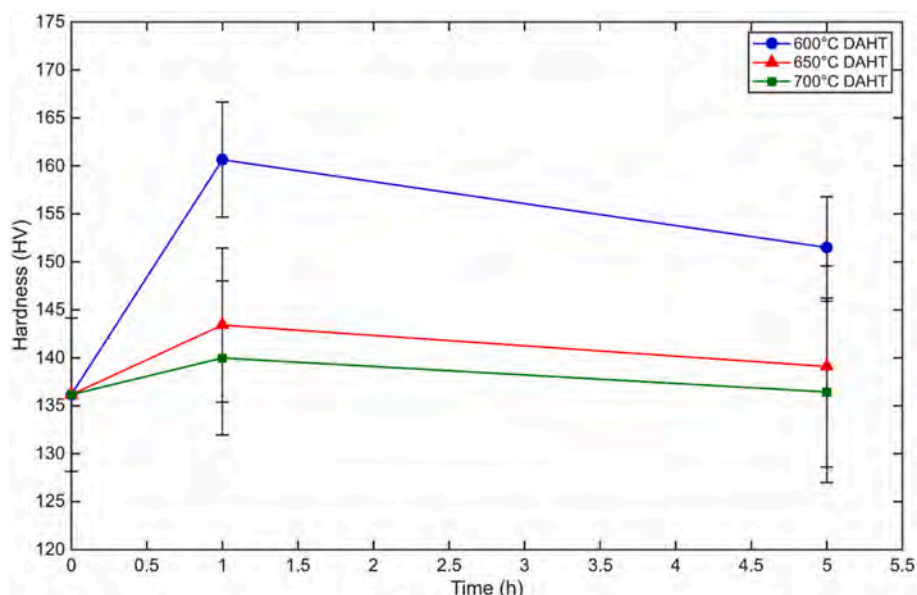


Fig. 11. Average microhardness of the different heat-treatment conditions tested, illustrating the influence of temperature and time on material strengthening.

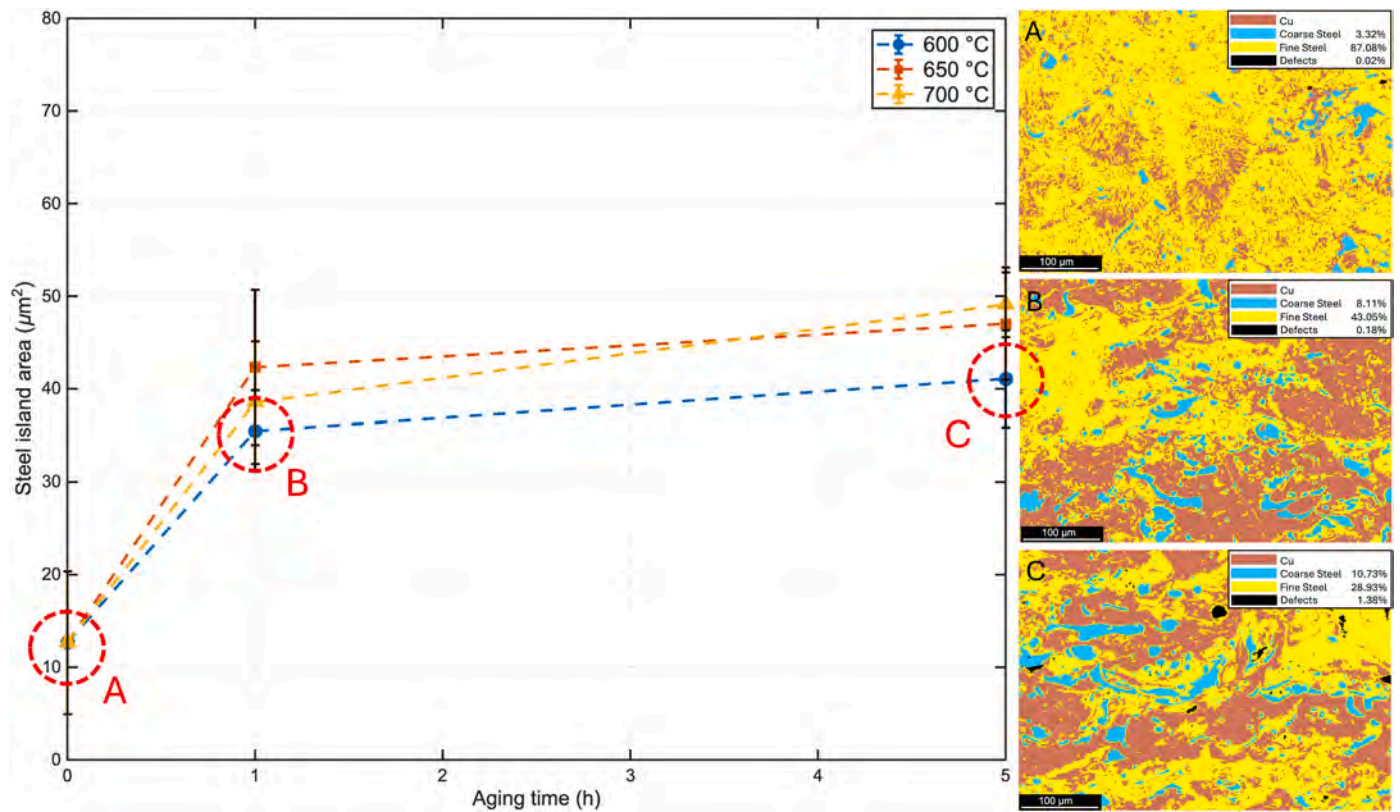


Fig. 13. Average steel-rich island area for the different aging conditions of the S6 samples, quantified by optical image segmentation. Representative segmented micrographs for the 600 °C condition are shown in the insets: (A) as-built, (B) 600 °C for 1 h, and (C) 600 °C for 5 h.

In the present system, the heterogeneity in hardness arises from the interplay between local phase distribution and solidification-driven refinement. Regions with a fine steel dispersion (Fig. 10d), which involve in refined grains morphology, exhibit higher hardness due to increased nucleation density and restricted grain growth. The limited grain growth, combined with the high density of phase boundaries, promotes the development of local lattice distortion, as confirmed by local increased KAM values (Fig. 7e), which also reflects enhanced local dislocation content, definitely contributing to dislocation strengthening.

Within the selected temperature range, the aging behaviour of the S6 samples observed after 1 h and 5 h of heat treatment is consistent with that typically reported for precipitation-hardening (PH) materials (Fig. 11). For all the investigated temperatures, hardness increases after 1 h of aging and decreases after longer thermal exposure (5h), reflecting the onset of an overaging-like behaviour, in which the reinforcing features lose their ability to effectively hinder dislocation motion and grain growth.

The most pronounced hardening effect is observed at 600 °C, while at higher temperatures, the hardening response progressively decreases, suggesting an acceleration of microstructural evolution and ripening phenomena.

Focusing on the 600 °C condition, the microstructure undergoes significant changes with increasing aging time. As visible in Fig. 12, corresponding to the peak-aged condition, the initially fine steel dispersion progressively transforms into larger steel-rich islands through a mechanism consistent with Ostwald ripening in close analogy to what is typically observed for precipitates in conventional PH alloys, hence suggesting active diffusion-driven microstructural rearrangement.

From a quantitative perspective, optical image segmentation analysis, the results of which are presented in Fig. 13, help reveal the progressive increase in size of the steel regions with increasing thermal exposure.

The average area of the coarser domains increases from

approximately 12 μm² in the as-built condition to nearly 49 μm² after the most severe thermal treatment. At the same time, the area fraction associated with the finer steel dispersion progressively decreases with aging time, halving after 1 h relative to the as-built condition and halving again after 5 h relative to the 1 h condition. As shown by the spatial distribution in the insets A, B, and C of Fig. 13, these residual fine features remain mainly confined to the surroundings of the larger islands.

Furthermore, the EBSD analysis of Fig. 14 remark this interpretation showing the effect on the grain growth. As the treatment time increases, the ultrafine-grained regions progressively disappear, giving way to a more homogeneous structure that resembles the surrounding columnar copper morphology. Solid-state diffusion, in fact, enhances phase separation and reduces the constraint effects that initially limited grain growth in the AB condition.

3.5. Thermal conductivity

Finally, thermal diffusivity was evaluated for the as-built S6_{IS}, S1_{IS} and S11_{IS} samples using the laser flash technique from ambient temperature up to 700 °C. Subsequently, ETC values were derived, following the procedure described in Section 2 (Fig. 15).

For all the studied samples, the ETC displayed overall comparable values, and a consistent enhancement with temperature, reaching on average a plateau of approximately 170 W/mK at 500 °C. This value is comparable to those reported for LPBF-produced structural copper alloys such as CuCrZr and CuCrNb in the as-built condition over a similar temperature range [61], [62].

The slightly higher ETC values observed for the edge-region samples at lower temperatures can be related to the coarser steel dispersion characteristic of these regions. According to effective medium theories incorporating interfacial thermal resistance, such as the Maxwell-Eucken or Hasselman-Johnson/Nan models [63], a coarser

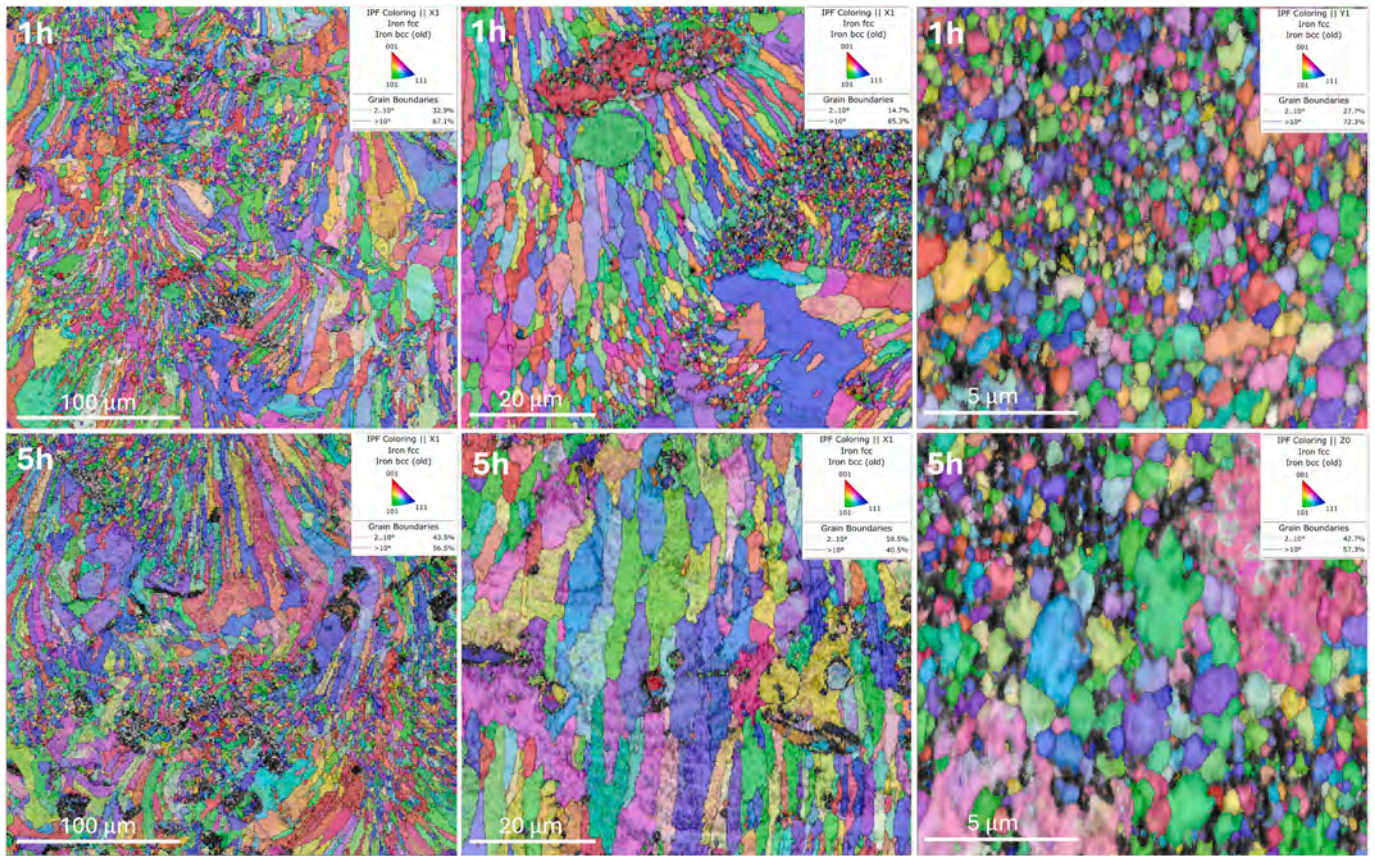


Fig. 14. IPF maps at different magnifications for the 600 °C condition, showing microstructural evolution after thermal exposure, showing the progressive disappearing of the initial bimodal microstructure toward a fully columnar morphology.

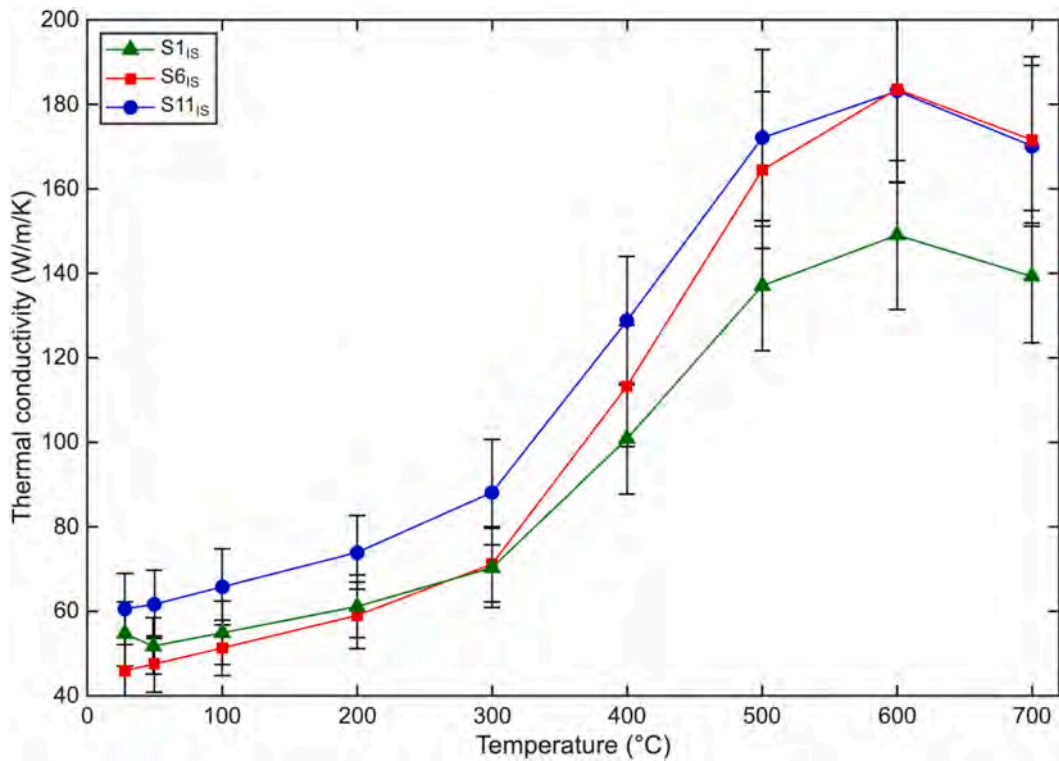


Fig. 15. Effective thermal conductivity (ETC) evolution of the S1_{IS}, S6_{IS}, and S11_{IS} as-built samples up to 700 °C.

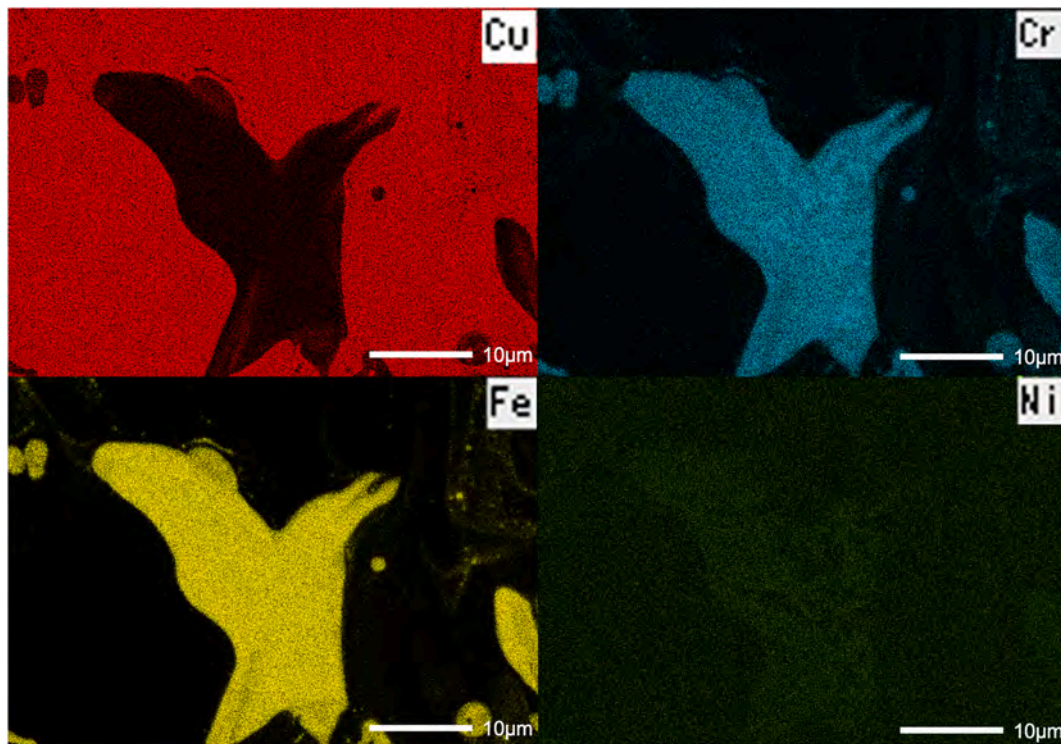


Fig. 16. EDS elemental map of sample 6_{WS} after 5h aging at 600 °C showing the coarsening of the steel phase with the consequent huge reduction of interfacial areas between the two materials.

second-phase dispersion reduces the overall Cu/steel interfacial area and therefore lowers the contribution of Kapitza resistance.

As the temperature increases, the ETC values tend to converge, consistently with the thermally activated coalescence and ripening phenomena of the steel phase. These diffusion-driven processes, quantitatively evidenced by the segmentation analysis reported in Fig. 13, promote the growth and consolidation of the dispersed steel phase, further reducing the Cu/steel interfacial area and the associated interfacial thermal resistance.

The only exception to this trend is represented by the S1_S sample, which exhibited an approximately 20% lower ETC at high temperature. This deviation can be attributed to the higher inherent defectiveness of this sample, as already pointed out in the previous sections (Fig. 5). Although the ETC measurements reported here were performed only on the as-built samples, additional evidence supporting the proposed mechanism are provided by the EDS elemental mapping of the most severely thermally treated condition (600 °C for 5 h), shown in Fig. 16. The EDS maps complement the segmentation analysis reported in Fig. 13 by providing higher-magnification chemical evidence of the steel phase distribution, including the finer steel dispersion that cannot be reliably resolved by optical image analysis.

The thermal transport, in this system, is dominated by the Cu matrix, whose conductivity is highly sensitive to electron scattering. During aging, diffusion-driven homogenization reduces residual solute atoms and lattice defects, while concurrent grain growth decreases the density of grain boundaries thereby increasing the electron mean free path. In accordance with Matthiessen rule, which states that the total scattering rate is the sum of contributions from phonons, impurities, and defects, and grain boundaries [64], this reduction enhances charge transport, directly involving in an increase of the ETC of the material. However, as coarsening progresses, a progressive strain field develops, accompanied by chemical discontinuities, ultimately leading to the slight reversion of the trend observed in ETC at high temperature.

4. Conclusions

A comprehensive investigation into the microstructural evolution, aging behavior, as well as the thermal and mechanical response of a novel Cu/17-4 PH multi-material system produced by LPBF through powder blending is presented in this study. The powder blending approach proved effective in enhancing the processability of copper, enabling the achievement of a high degree of densification (residual porosity below 1%). Moreover, the resulting material properties are highly promising for the intended application, suggesting that powder mixing can serve as an effective strategy for tailoring microstructures in LPBF based aerospace manufacturing. The key findings are summarized as follows:

- Despite identical processing parameters, a pronounced position-dependent behavior was observed across the build platform. This was attributed to spatial variations in the effective energy input arising from the optical system. The central regions experienced higher absorbed energy, favoring a transition to the keyhole regime. This condition enhanced Marangoni-driven convection and melt pool turbulence, resulting in a finer dispersion of the steel phase within the Cu-rich matrix. In contrast, the outer regions, dominated by conduction-mode melting, exhibited coarser phase segregation with larger steel domains.
- The spatial heterogeneity in phase distribution strongly influenced solidification behavior. Regions characterized by a fine steel dispersion exhibited a high density of interfaces, which promoted heterogeneous nucleation. This disrupted epitaxial grain growth and led to a refined, predominantly equiaxed microstructure.
- The mechanical response, evaluated through microhardness and nanoindentation mapping, mirrored this microstructural variability. A clear spatial gradient in hardness was observed, with higher values and lower scatter in the central regions of the build platform. This behavior can be ascribed to the combined effects of grain refinement

(Hall-Petch strengthening), increased interface density, and localized dislocation strengthening.

- The thermal evolution of the material is strongly influenced by the complex thermal history inherent to LPBF processing. The initially fine steel dispersion acts as a population of dispersoids that, upon thermal aging, coarsen via an Ostwald ripening mechanism, leading to pronounced phase separation.
- The evolution of effective thermal conductivity (ETC) can be rationalized using effective medium models that incorporate interfacial thermal resistance (e.g., Maxwell-Eucken or Hasselman-Johnson/Nan approaches). Heat treatment promotes diffusion-driven coalescence and growth of the steel phase, reducing the Cu/steel interfacial area and, consequently, the associated Kapitza resistance.

Declaration of competing interest

The authors declare that they have no known competing financial interests or personal relationships that could have appeared to influence the work reported in this paper.

Acknowledgments

The authors gratefully thank ASI (Italian Space Agency) for financial support of PhD research activity (of Matteo Crachi) which lead to part of the present results.

The authors would like to acknowledge Sòphia High Tech s.r.l. for the production of the samples used in this study. The authors also gratefully acknowledge Francesca Caltagirone for their contribution to some of the characterization presented in this work.

Data availability

Data will be made available on request.

References

- Pizzarelli M. An algebraic model for structural and life analysis of regeneratively-cooled thrust chambers. *J Propul Power* mar. 2020;36(2):191–201. <https://doi.org/10.2514/1.B37669>. fasc.
- Sutton GP. *HISTORY of Liquid Propellant Rocket Engines*. Reston, VA: American Institute of Aeronautics and Astronautics; 2006. <https://doi.org/10.2514/4.868870>.
- Li C, Wei e L. Recent progress and scientific challenges in multi-material additive manufacturing via laser-based powder bed fusion. *Virtual Phys Prototyp mag*. 2021;16(3):347–71. <https://doi.org/10.1080/17452759.2021.1928520>. fasc.
- Zhang H, Jin X, Xiao Z, Yao e L. Mechanical properties and interfacial characterization of additive-manufactured CuZrCr/CoCrMo multi-metals fabricated by powder bed fusion using pulsed wave laser. *Micromachines giu*. 2024;15(6):765. <https://doi.org/10.3390/mi15060765>. fasc.
- Nazir A, et al. Multi-material additive manufacturing: a systematic review of design, properties, applications, challenges, and 3D printing of materials and cellular metamaterials. *Mater Des feb*. 2023;226:111661. <https://doi.org/10.1016/j.matdes.2023.111661>.
- Li Y, et al. A review on functionally graded materials and structures via additive manufacturing: from multi-scale design to versatile functional properties. *Adv Mater Technol giu*. 2020;5(6):1900981. <https://doi.org/10.1002/admt.201900981>. fasc.
- Hasanov S, et al. Review on additive manufacturing of multi-material parts: progress and challenges. *J Manuf Mater Process dic*. 2021;6(1):4. <https://doi.org/10.3390/jmmp6010004>. fasc.
- Schwighamer RJ. Materials and processes for shuttle engine, external tank, and solid rocket booster. In: *A New Era in Space Transportation*. Elsevier; 1977. p. 71–88. <https://doi.org/10.1016/B978-0-08-021710-9.50013-6>.
- Wang D, et al. Recent progress on additive manufacturing of multi-material structures with laser powder bed fusion. *Virtual Phys Prototyp apr*. 2022;17(2):329–65. <https://doi.org/10.1080/17452759.2022.2028343>. fasc.
- Neirink B, Li X, Hick e M. Powder deposition systems used in powder bed-based multimetal additive manufacturing. *Acc Mater Res giu*. 2021;2(6):387–93. <https://doi.org/10.1021/accounts.mr1c00030>. fasc.
- Grabl PR, Protz DCS, Ellis DDL, Greene e SE. Progress in additively manufactured copper-alloy GRCo-84, GRCo-42, and bimetallic combustion chambers for liquid rocket engines. In: *Th International Astronautical Congress*. Washington, DC: International Astronautical Federation (IAF-HQ), ott; 2019 [Online]. Disponibile su: <https://ntrs.nasa.gov/citations/20190033311>.
- Zheng B, Zhou Y, Smugeresky JE, Schoenung JM, Lavernia e EJ. Thermal behavior and microstructure evolution during laser deposition with laser-engineered net shaping: part II. Experimental investigation and discussion. *Mettall Mater Trans A set*. 2008;39(9):2237–45. <https://doi.org/10.1007/s11661-008-9566-6>. fasc.
- Grabl PR, et al. Lightweight thrust chamber assemblies using multi-alloy additive manufacturing and composite overwrap. In: *AIAA Propulsion and Energy 2020 Forum, Virtual Event*. American Institute of Aeronautics and Astronautics; ago. 2020. <https://doi.org/10.2514/6.2020-3787>.
- Grabl PR, Teasley TW, Protz CS, Garcia MB, Ellis D, Kantzos e C. Advancing GRCo-based bimetallic additive manufacturing to optimize component design and applications for liquid rocket engines. In: *AIAA Propulsion and Energy 2021 Forum, Virtual Event*. American Institute of Aeronautics and Astronautics; ago; 2021. <https://doi.org/10.2514/6.2021-3231>.
- Mao S, Zhang DZ, Ren Z, Fu G, Ma e X. Effects of process parameters on interfacial characterization and mechanical properties of 316L/CuCrZr functionally graded material by selective laser melting. *J Alloys Compd apr*. 2022;899:163256. <https://doi.org/10.1016/j.jallcom.2021.163256>.
- Mao S, Yang B, Liu G, Liu G, Zhang e Z. Temperature distribution and residual stress evolution at the interface of CuCrZr/316 L multi-material by laser powder bed fusion. *Opt Laser Technol ago*. 2023;163:109355. <https://doi.org/10.1016/j.optlastec.2023.109355>.
- Tucker M, Bambach e MR. Laser powder bed fusion of planar bi-metallic thermally auxetic lattice structures. *CIRP Ann* 2024;73(1):141–4. <https://doi.org/10.1016/j.cirp.2024.04.023>. fasc.
- Li X, Sukhomlinov D, Que e Z. Microstructure and thermal properties of dissimilar M300-CuCr1Zr alloys by multi-material laser-based powder bed fusion. *Int J Miner Metall Mater gen*. 2024;31(1):118–28. <https://doi.org/10.1007/s12613-023-2747-x>. fasc.
- Li X, Pan Z, Smolej L, Karthik Nadimpalli V, Moshiri e M. Towards manufacturing intra-layer multi-material mould tools with vertical interfaces using laser-based powder bed fusion. *Mater Des lug*. 2024;243:113056. <https://doi.org/10.1016/j.matdes.2024.113056>.
- Wei C, Sun Z, Huang Y, Li e L. Embedding anti-counterfeiting features in metallic components via multiple material additive manufacturing. *Addit Manuf dic*. 2018;24:1–12. <https://doi.org/10.1016/j.addma.2018.09.003>.
- Bai Y, Zhang J, Zhao C, Li C, Wang e H. Dual interfacial characterization and property in multi-material selective laser melting of 316L stainless steel and C52400 copper alloy. *Mater Charact set*. 2020;167:110489. <https://doi.org/10.1016/j.matchar.2020.110489>.
- Al-Jamal OM, Hinduja S, Li e L. Characteristics of the bond in Cu–H13 tool steel parts fabricated using SLM. *CIRP Ann* 2008;57(1):239–42. <https://doi.org/10.1016/j.cirp.2008.03.010>. fasc.
- Liu L, et al. Interfacial characteristics and formation mechanisms of copper–steel multimaterial structures fabricated via laser powder bed fusion using different building strategies. *Chin J Mech Eng Addit Manuf Front set*. 2022;1(3):100045. <https://doi.org/10.1016/j.cjmeam.2022.100045>. fasc.
- Karakaya İ. «ASM Handbook Volume 3 Alloy Phase Diagrams». *ASM International, ASM International*; 2001.
- Rauh S, et al. Laser powder bed fusion of copper–tungsten composites for heat sink applications in high-power electronics. *Adv Eng Mater feb*. 2026:e202502052. <https://doi.org/10.1002/adem.202502052>.
- Morozov EA, Ablyaz TR, Muratov KR, Shlykov ES, Smolentsev e EV. Laser hardening of copper-iron pseudoalloy. *Eng Solid Mech* 2020;83–92. <https://doi.org/10.5267/j.esm.2019.10.006>.
- Zvereva OS, Dovydenkov VA, Alibekov S Ya, Razinskaya e OI. Technology of producing pseudo alloys of system fine porous powder steel-copper alloy by the infiltration method. *Inorg Mater Appl Res lug*. 2021;12(4):922–7. <https://doi.org/10.1134/S2075113321040456>. fasc.
- Dyachkova LN. Structure and properties of antifriction pseudo-alloys of the powder steel–copper alloy, infiltrated with materials of various compositions. *J Frict Wear ago*. 2023;44(4):197–203. <https://doi.org/10.3103/S1068366623040050>. fasc.
- Liu ZH, Zhang DQ, Sing SL, Chua CK, Loh e LE. Interfacial characterization of SLM parts in multi-material processing: metallurgical diffusion between 316L stainless steel and C18400 copper alloy. *Mater Charact ago*. 2014;94:116–25. <https://doi.org/10.1016/j.matchar.2014.05.001>.
- Luscinì D, Crachi M, Sesana R, Delprete C, Sicignano e N. Experimental analysis of thermomechanical properties of innovative heat treated metal matrix composites processed by additive manufacturing for space rocket applications. *J Mater Eng Perform set*. 2025;34(17):19824–39. <https://doi.org/10.1007/s11665-025-11165-x>. fasc.
- Crachi M, et al. Experimental characterization of a new L-PBF AM 65% copper - 35% maraging steel metal-matrix-composite for liquid rocket engine thrust chambers. *Mater Today Commun apr*. 2025;45:112146. <https://doi.org/10.1016/j.mtcomm.2025.112146>.
- Mirzababaei S, et al. Remarkable enhancement in thermal conductivity of stainless-steel leveraging metal composite via laser powder bed fusion: 316L-Cu composite. *Addit Manuf mag*. 2023;70:103576. <https://doi.org/10.1016/j.addma.2023.103576>.
- Hasselman DPH, Johnson e LF. Effective thermal conductivity of composites with interfacial thermal barrier resistance. *J Compos Mater giu*. 1987;21(6):508–15. <https://doi.org/10.1177/002199838702100602>. fasc.
- Pietrak e K, Wisniewski TS. *Methods for Experimental Determination of Solid-Solid Interfacial Thermal Resistance with Application to Composite Materials*. 2014.
- Pohl ET Swartz e RO. Thermal boundary resistance. *Rev Mod Phys lug*. 1989;61(3):605–68. <https://doi.org/10.1103/RevModPhys.61.605>. fasc.

- [36] J. Whiting, B. Lane, K. Chou, e B. Cheng, «Thermal property measurement methods and analysis for additive manufacturing solids and powders».
- [37] Porter AS Sabau e WD. Alloy shrinkage factors for the investment casting of 17-4PH stainless steel parts. *Metall Mater Trans B* apr. 2008;39(2):317–30. <https://doi.org/10.1007/s11663-007-9125-3>. fasc.
- [38] Aghayar Y, et al. Laser powder bed fusion of pure copper electrodes. *Mater Des* mar. 2024;239:112742. <https://doi.org/10.1016/j.matdes.2024.112742>.
- [39] Carr RL. Evaluating flow properties of solids. *Chem Eng* 1965;72:163–8.
- [40] Crachi M, et al. Effect of LPBF process parameters on thermomechanical properties of a copper-based metal matrix composite. *J Manuf Sci Eng ott*. 2025;147(10):101009. <https://doi.org/10.1115/1.4069275>. fasc.
- [41] E37 Committee, Test Method for Determining Specific Heat Capacity by Sinusoidal Modulated Temperature Differential Scanning Calorimetry. doi: 10.1520/E2716-23.
- [42] Metallic materials. Instrumented indentation test for hardness and materials parameters test method, EN ISO 14577-1:2015 [Online]. Disponibile su: <https://www.iso.org/foreword-supplementary-information.html>; 2015.
- [43] Kleszczynski S, Ladewig A, Friedberger K, zur Jacobsmühlen J, Herhof D, Witt e G. Position dependency of surface roughness in parts from laser beam melting systems. In: Presentato al 26th International Solid Free Form Fabrication (SFF) Symposium. Austin, TX: University of Texas at Austin, ago; 2015. p. 360–70 [Online]. Disponibile su: <https://hdl.handle.net/2152/89333>.
- [44] Fathi-Hafshejani P, Soltani-Tehrani A, Shamsaei N, Mahjouri-Samani e M. Laser incidence angle influence on energy density variations, surface roughness, and porosity of additively manufactured parts. *Addit Manuf* feb. 2022;50:102572. <https://doi.org/10.1016/j.addma.2021.102572>.
- [45] Li E, Shen H, Wang L, Wang G, Zhou e Z. Laser shape variation influence on melt pool dynamics and solidification microstructure in laser powder bed fusion. *Addit Manuf Lett* lug. 2023;6:100141. <https://doi.org/10.1016/j.addlet.2023.100141>.
- [46] Tang X, Chen X, Sun F, Liu P, Zhou H, Fu e S. The current state of CuCrZr and CuCrNb alloys manufactured by additive manufacturing: a review. *Mater Des* dic. 2022;224:111419. <https://doi.org/10.1016/j.matdes.2022.111419>.
- [47] Zhang L-J, Zhang G-F, Ning J, Zhang X-J, Zhang e J-X. Microstructure and properties of the laser butt welded 1.5-mm thick T2 copper joint achieved at high welding speed. *Mater Des* dic. 2015;88:720–36. <https://doi.org/10.1016/j.matdes.2015.09.072>.
- [48] Kelton KF, Greer AL. Heterogeneous nucleation. *Pergamon Mater Series* 2010;15:165–226. [https://doi.org/10.1016/S1470-1804\(09\)01506-5](https://doi.org/10.1016/S1470-1804(09)01506-5). Elsevier.
- [49] Wang M-J, Zhang G-W, Xu H, Dong Y, Sun F-E, Fu e Y-Z. Density functional theory investigation on the stability, adhesion strength, tensile properties and fracture behavior of γ -Fe/Cu heterogeneous nucleation interface. *Results Phys* mag. 2021;24:104143. <https://doi.org/10.1016/j.rinp.2021.104143>.
- [50] Liu Y, et al. Laser powder bed fusion of copper matrix iron particle reinforced nanocomposite with high strength and high conductivity. *J Mater Sci Technol* gen. 2023;134:50–9. <https://doi.org/10.1016/j.jmst.2022.06.007>.
- [51] Peng W-Q, Li Q, Xu Y-P, Zhou H-S, Luo e G-N. Achieving novel copper–steel joints with a combination of high strength and ductility reinforced by in-situ Fe-rich particles. *J Mater Sci Technol* mag. 2024;182:231–45. <https://doi.org/10.1016/j.jmst.2023.09.036>.
- [52] Geng S, Jiang P, Shao X, Guo L, Gao e X. Heat transfer and fluid flow and their effects on the solidification microstructure in full-penetration laser welding of aluminum sheet. *J Mater Sci Technol* giu. 2020;46:50–63. <https://doi.org/10.1016/j.jmst.2019.10.027>.
- [53] Xu X, Tang C, Wang H, An Y, Zhao e Y. Microstructure evolution and grain refinement mechanism of rapidly solidified single-phase copper based alloys. *J Mater Sci Technol* nov. 2022;128:160–79. <https://doi.org/10.1016/j.jmst.2022.04.025>.
- [54] Xu XL, Zhao YH, Hou e H. Growth velocity-undercooling relationship and structure refinement mechanism of undercooled Ni-Cu alloys. *J Alloys Compd* gen. 2019;773:1131–40. <https://doi.org/10.1016/j.jallcom.2018.09.228>.
- [55] Xu X, Zhao Y, Hou H, Liu e F. Concentration and fluid flow effects on kinetics, dendrite remelting and stress accumulation upon rapid solidification of deeply undercooled alloys. *J Alloys Compd* mag. 2018;744:740–9. <https://doi.org/10.1016/j.jallcom.2018.02.065>.
- [56] Rowolt C, Milkereit B, Springer A, Kreyenschulte C, Kessler e O. «Dissolution and precipitation of copper-rich phases during heating and cooling of precipitation-hardening steel X5CrNiCuNb16-4 (17-4 PH). *J Mater Sci* set. 2020;55(27):13244–57. <https://doi.org/10.1007/s10853-020-04880-4>. fasc.
- [57] Milkereit B, et al. On the precipitation and transformation kinetics of precipitation-hardening steel X5CrNiCuNb16-4 in a wide range of heating and cooling rates. *Materialia* dic. 2024;38:102254. <https://doi.org/10.1016/j.mtla.2024.102254>.
- [58] Maharana P, et al. Corrosion behavior of 17–4 PH stainless steel manufactured by laser powder bed fusion: effect of graphene coating and heat-treatment. *Mater Today Commun* dic. 2024;41:111098. <https://doi.org/10.1016/j.mtcomm.2024.111098>.
- [59] Christien F, Telling MTF, Knight e KS. A comparison of dilatometry and in-situ neutron diffraction in tracking bulk phase transformations in a martensitic stainless steel. *Mater Charact* ago. 2013;82:50–7. <https://doi.org/10.1016/j.matchar.2013.05.002>.
- [60] Turchanin MA, Agraval PG, Abdulov e AR. Phase equilibria and thermodynamics of binary copper systems with 3d-metals. VI. Copper-nickel system. *Powder Metall Met Ceram* set. 2007;46(9–10):467–77. <https://doi.org/10.1007/s11106-007-0073-x>. fasc.
- [61] Barbosa A, et al. Powder bed fusion laser beam (PBF-LB) of GRCop42. Processability and influence of post-build heat treatments on the microstructure and thermal and mechanical properties. In: Euro PM2025 Proceedings, EPMA, Set; 2025. <https://doi.org/10.59499/EP256779205>.
- [62] Biffi CA, Flocchi J, Boldrini S, Tuissi e A. CuCrZr alloy manufactured by LPBF process: correlation between microstructure, mechanical and thermal properties. *Lasers Manuf Mater Process* mar. 2024;11(1):143–53. <https://doi.org/10.1007/s40516-023-00240-7>.
- [63] Pietrak e K, Wisniewski TS. *A Review of Models for Effective Thermal Conductivity of Composite Materials*. 2015.
- [64] Bass J. Deviations from Matthiessen's rule. *Adv Phys* mag. 1972;21(91):431–604. <https://doi.org/10.1080/00018737200101308>. fasc.